Article

A few-layer covalent network of fullerenes

https://doi.org/10.1038/s41586-022-05401-w

Received: 6 June 2022

Accepted: 30 September 2022

Published online: 4 January 2023

Check for updates

Elena Meirzadeh[1]✉, Austin M. Evans[1,2], Mehdi Rezaee[3], Milena Milich[4], Connor J. Dionne[5], Thomas P. Darlington[6], Si Tong Bao[1], Amymarie K. Bartholomew[1], Taketo Handa[1], Daniel J. Rizzo[7], Ren A. Wiscons[8], Mahniz Reza[9], Amirali Zangiabadi[10], Natalie Fardian-Melamed[6], Andrew C. Crowther[9], P. James Schuck[6], D. N. Basov[7], Xiaoyang Zhu[1], Ashutosh Giri[5], Patrick E. Hopkins[4,11,12], Philip Kim[13], Michael L. Steigerwald[1]✉, Jingjing Yang[1]✉, Colin Nuckolls[1]✉ & Xavier Roy[1]✉

The two natural allotropes of carbon, diamond and graphite, are extended networks of sp^3-hybridized and sp^2-hybridized atoms, respectively[1]. By mixing different hybridizations and geometries of carbon, one could conceptually construct countless synthetic allotropes. Here we introduce graphullerene, a two-dimensional crystalline polymer of C_{60} that bridges the gulf between molecular and extended carbon materials. Its constituent fullerene subunits arrange hexagonally in a covalently interconnected molecular sheet. We report charge-neutral, purely carbon-based macroscopic crystals that are large enough to be mechanically exfoliated to produce molecularly thin flakes with clean interfaces—a critical requirement for the creation of heterostructures and optoelectronic devices[2]. The synthesis entails growing single crystals of layered polymeric $(Mg_4C_{60})_\infty$ by chemical vapour transport and subsequently removing the magnesium with dilute acid. We explore the thermal conductivity of this material and find it to be much higher than that of molecular C_{60}, which is a consequence of the in-plane covalent bonding. Furthermore, imaging few-layer graphullerene flakes using transmission electron microscopy and near-field nano-photoluminescence spectroscopy reveals the existence of moiré-like superlattices[3]. More broadly, the synthesis of extended carbon structures by polymerization of molecular precursors charts a clear path to the systematic design of materials for the construction of two-dimensional heterostructures with tunable optoelectronic properties.

C_{60} fullerene, the first synthetic carbon allotrope[4,5], is a geometrically closed, polycyclic polymer composed solely of carbon atoms (Fig. 1a). This polymer is infinite in the literal sense of not having any termini, but it is obviously quite finite in being the size of a normal, albeit large, molecule. Graphene, another allotrope of elemental carbon[6], is also a polymer of carbon atoms, but in this case, the polymerization leads to a geometrically open result: infinite, two-dimensional (2D) sheets (Fig. 1b). Here we disclose a 2D polymer of C_{60}, which we synthesize by linking C_{60} molecules into layered, graphene-like hexagonal sheets (Fig. 1c). By analogy to graphene and graphite, we have dubbed this material graphullerene, and its three-dimensional van der Waals (vdW) solid, graphullerite.

Our chemical strategy to prepare graphullerene was inspired by a recent study[7], which used the chemical vapour transport (CVT) approach to grow single crystals of metal-doped polyfullerides. First, we grow single crystals of magnesium (Mg)-doped polyfulleride—$(Mg_4C_{60})_\infty$. These polyfullerides are obtained by pressing a pellet of C_{60} and Mg powder under an inert atmosphere, sealing it in a fused silica tube under vacuum, and placing it in a horizontal furnace with a temperature gradient (Fig. 2a). Large, black, hexagonal crystals (hundreds of micrometres in lateral dimensions), with a metallic luster, are obtained at the cold end of the tube (Fig. 2b).

Single-crystal X-ray diffraction (SCXRD) reveals that the crystals have a layered structure, and display a quasi-hexagonal lattice, with each C_{60} forming eight covalent σ bonds to six neighbours within a molecular plane. Four of these make single connections between the C_{60} molecules, and each of the other two pairs doubly connects the C_{60} molecules (Fig. 2c). The synthesis yields highly reduced sheets with four Mg counterions per fullerene. The counterions are closely associated with each individual layer (Fig. 2c), and not shared between layers; hence, the layers are only weakly bonded to each other, predominantly through vdW interactions. Single crystals of $(Mg_4C_{60})_\infty$ were also grown in a recent study[8] using a similar CVT approach.

We fabricated mesoscopic devices to investigate the electrical transport properties of these highly reduced polymerized fullerene sheets. We produced thin bulk flakes of $(Mg_4C_{60})_\infty$ by mechanical exfoliation

[1]Department of Chemistry, Columbia University, New York, NY, USA. [2]George and Josephine Butler Polymer Research Laboratory, Center for Macromolecular Science and Engineering, Department of Chemistry, University of Florida, Gainesville, FL, USA. [3]School of Engineering and Applied Sciences, Harvard University, Cambridge, MA, USA. [4]Department of Mechanical and Aerospace Engineering, University of Virginia, Charlottesville, VA, USA. [5]Department of Mechanical, Industrial and Systems Engineering, University of Rhode Island, Kingston, RI, USA. [6]Department of Mechanical Engineering, Columbia University, New York, NY, USA. [7]Department of Physics, Columbia University, New York, NY, USA. [8]Department of Chemistry, Amherst College, Amherst, MA, USA. [9]Department of Chemistry, Barnard College, New York, NY, USA. [10]Department of Applied Physics and Applied Mathematics, Columbia University, New York, NY, USA. [11]Department of Materials Science and Engineering, University of Virginia, Charlottesville, VA, USA. [12]Department of Physics, University of Virginia, Charlottesville, VA, USA. [13]Department of Physics, Harvard University, Cambridge, MA, USA. ✉e-mail: em3428@columbia.edu; mls2064@columbia.edu; yjj0412@berkeley.edu; cn37@columbia.edu; xr2114@columbia.edu

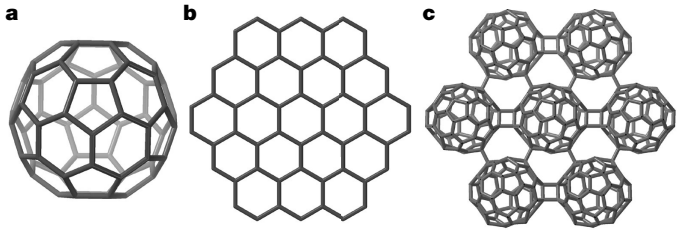

Fig. 1 | Carbon allotropes. a,**b**, C_{60} fullerene, a zero-dimensional molecular cage composed of 60 carbon atoms (**a**), and graphene, consisting of a single layer of atoms (**b**), both composed of three-coordinate carbon. **c**, Graphullerene, a molecular sheet of carbon assembled from covalently linked C_{60} fullerene superatomic building blocks.

and deposited gold contacts using the dry-transfer and high-resolution stencil mask technique (an approximately 70-nm-thick device is shown in the inset of Fig. 2d). $(Mg_4C_{60})_\infty$ exhibits thermally activated transport along the in-plane direction (Extended Data Fig. 1) with an activation energy of 121 meV, as calculated from fitting an Arrhenius thermal activation model (Fig. 2d).

One of the key benefits of 2D materials prepared by mechanical exfoliation of vdW crystals is their ultra-clean surfaces without counterions or contaminants. This is critical for many applications, and in particular for the assembly of heterostructures and optoelectronic devices[3]. To create a vdW C_{60} polymer material that can be mechanically exfoliated, we attempted to remove the Mg from the $(Mg_4C_{60})_\infty$ lattice by immersing the crystals in different aqueous acidic solutions, expecting Mg to form water-soluble salts with the conjugate bases. Suspending $(Mg_4C_{60})_\infty$ in dilute aqueous solutions of acetic acid or nitric acid leaches out most of the Mg, yielding $(Mg_{0.5}C_{60})_\infty$, as determined by energy-dispersive X-ray spectroscopy (EDS). By suspending the $(Mg_{0.5}C_{60})_\infty$ crystals in *N*-methylpyrrolidone at 180 °C, we completely remove the Mg counterions (Fig. 3a). Upon examining the graphullerite crystals using scanning electron microscopy (SEM), we find that the crystals remain intact following Mg deintercalation (Fig. 3a, inset). With Mg taken out, the remaining material is entirely and purely carbon, yet it is not C_{60}; it is a vdW solid, graphullerite ($(C_{60})_\infty$ in the figures). We note that the lack of long-range registry of the covalent layers along the stacking direction, indicated by the broadening of the powder X-ray diffraction (PXRD) peaks (Extended Data Fig. 2), has thus far prevented structural determination using SCXRD.

Raman spectroscopy is a diagnostic probe of C_{60} polymerization[9,10], and when we compare the Raman spectrum of graphullerite to that of molecular C_{60}, we find a splitting of the C_{60} H_g modes at 1,420 cm^{-1} and 1,560 cm^{-1} (Extended Data Fig. 3a), which is attributed to the lower symmetry of polymerized C_{60}. Furthermore, the $A_g(2)$ pentagonal pinch mode at 1,469 cm^{-1}, characteristic of molecular C_{60}, is not observed in graphullerite. Quenching of the most intense $A_g(2)$ mode corroborates the high degree of polymerization[11]. An alternative interpretation of the Raman spectrum is that the $A_g(2)$ mode is shifted to a lower energy as a result of the polymerization[12] and overlaps with the broad $H_g(7)$ mode at 1,420 cm^{-1}. The Raman spectra of $(Mg_4C_{60})_\infty$ and graphullerite show no significant differences, indicating that the covalent bonding between fullerene subunits is retained in graphullerite despite the complete removal of the Mg. Note that the $H_g(7)$ mode of bilayer graphullerene, obtained by mechanical exfoliation (described below), is slightly shifted to higher energy compared with bulk graphullerite (Extended Data Fig. 3a).

To test whether the Mg counterions, which constitute the scaffolding for the construction of graphullerite, are essential for the thermal stability of the structure, we performed differential scanning calorimetry (DSC) and thermogravimetric analysis (TGA) measurements on graphullerite and $(Mg_4C_{60})_\infty$ crystals. The DSC shows no endothermic peak up to about 550 °C, and no mass loss occurs up to about 700 °C, as determined by TGA (Extended Data Fig. 4). PXRD measurements, however, show that although graphullerite crystals are structurally stable up to 400 °C, they depolymerize and crystallize as molecular C_{60} when heated to 500 °C for 1 h (Extended Data Fig. 5). Furthermore, the characteristic $A_g(2)$ mode for molecular C_{60} at 1,469 cm^{-1} appears in the Raman spectra of the annealed crystals (Extended Data Fig. 3b). The absence of an endothermic peak in the DSC data suggests that depolymerization is a gradual process, hard to capture by calorimetry.

In as much as there appears to be no interlayer C–C covalent links in graphullerite, we suspected that we could exfoliate the crystals down to a few layers, as in the case of graphite[6]. Indeed, mechanical exfoliation of graphullerite routinely produces uniform flakes as thin as bilayers with lateral dimensions on the order of tens of micrometres. Figure 3b,c shows the optical micrograph and atomic force microscopy (AFM) image of a bilayer. A recent study[8] obtained ionic monolayers of $[(NBu_4^+)_6(C_{60}^{6-})]_\infty$ from $(Mg_4C_{60})_\infty$ crystals via cationic exchange of Mg with tetrabutylammonium (NBu_4^+) cations, followed by solution exfoliation. The presence of counterions associated with the reduced sheets precludes the creation of clean, high-quality interfaces for the fabrication of optoelectronic devices and 2D heterostructures. This recent study[8] demonstrated that the ionic sheets can be neutralized

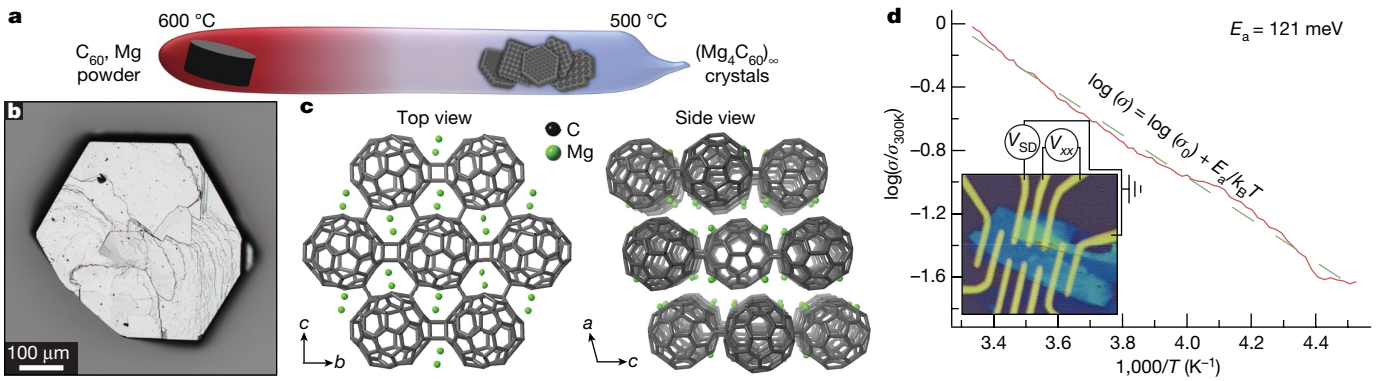

Fig. 2 | Synthesis and crystal structures of $(Mg_4C_{60})_\infty$. a, Schematic of the CVT technique used for the growth of $(Mg_4C_{60})_\infty$ single crystals. **b**, Optical micrograph of a single crystal. **c**, Crystal structure of $(Mg_4C_{60})_\infty$ showing a top view of a single layer and a side view emphasizing the stacking of the layers along the *a* axis. The C_{60} units within each layer are much closer to one another than they are in molecular C_{60} crystals[5]. The closest C···C distance between two C_{60} subunits (1.573(1) Å) is roughly half of that in molecular C_{60} (3.116 Å). This very close spacing between the fullerenes is a direct reflection of covalent bonding between the molecules. **d**, The log of the conductance (σ) versus temperature (T) for a 70-nm-thick $(Mg_4C_{60})_\infty$ device. A fit to a thermally activated (Arrhenius) model is given by the dashed green line. A typical device and corresponding four-terminal measurement scheme are shown in the inset. E_a, activation energy; k_B, Boltzmann constant; V_{SD}, source-drain voltage; V_{xx}, longitudinal voltage drop.

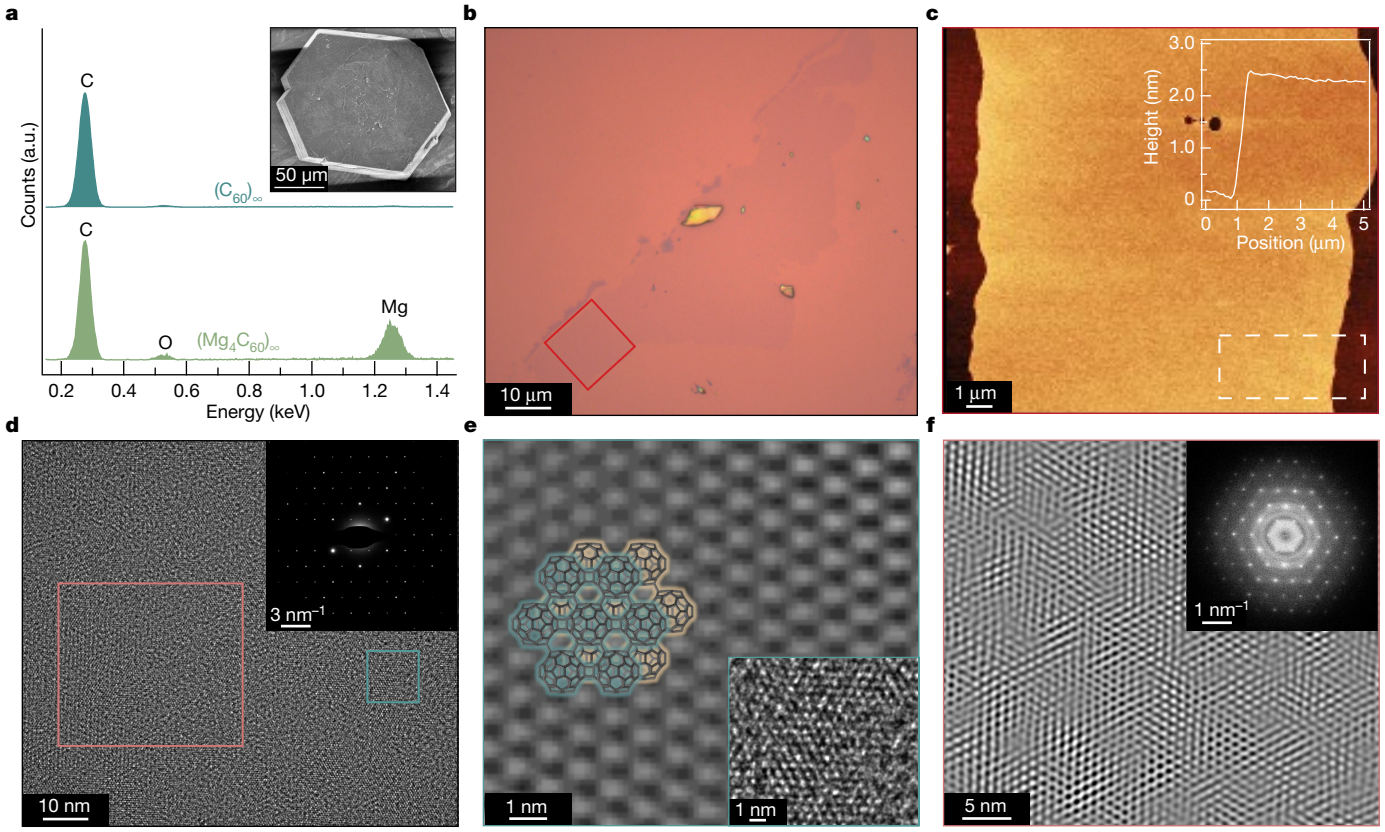

Fig. 3 | Mg deintercalation and mechanical exfoliation to produce graphullerene. a, Elemental composition of single crystals before ($(Mg_4C_{60})_\infty$) and after ($(C_{60})_\infty$) treatment with a dilute acetic acid solution, as determined by EDS. The absence of the oxygen peak in the spectrum of graphullerite implies that the observed oxygen peak in $(Mg_4C_{60})_\infty$ crystals corresponds to oxidized Mg species and not the fullerene sheets. Inset: SEM image of a graphullerite crystal. **b**, Optical micrograph of mechanically exfoliated graphullerene. **c**, AFM image of the bilayer selected in red in **b**. Inset, height profile measured over the region defined by the white dashed box. A 2.4-nm step height characteristic of bilayer graphullerene is observed. **d**, TEM image of a few-layer graphullerene flake prepared by mechanical exfoliation on a TEM grid. Inset: selected area electron diffraction pattern from a 100 × 100-nm^2 region of the flake. A low-magnification TEM image of this flake is shown in Extended Data Fig. 7. **e**, iFFT of the area selected in blue in **d**, which is magnified in the inset. The filtering removes the aperiodic pixel noise and represents the lattice superstructure, showing that each C_{60} is connected to six neighbouring fullerenes in a molecular plane. **f**, iFFT image of the area selected in pink in **d**. The high degree of crystallinity can be observed in the Fourier transform (inset) and the electron diffraction pattern in **d**.

using hydrogen peroxide; however, solvent residue resulting from solution exfoliation continues to be a problem in the field. In contrast, we present a simple preparation and the properties of the charge-neutral (Extended Data Fig. 6), mechanically exfoliatable graphullerene sheets.

The ability to exfoliate thin flakes allows us to directly image graphullerene using high-resolution transmission electron microscopy (HR-TEM) (Fig. 3d and Extended Data Fig. 7). Selected area electron diffraction of a few-layer flake shows that, despite the lack of long-range registry along the stacking direction, the flakes are highly crystalline within a molecular plane (Fig. 3d, inset). The magnified HR-TEM image shows bright spheres, corresponding to the C_{60} subunits, which are arranged in a hexagonal lattice (Fig. 3e, inset), as anticipated from the SCXRD structure of a single layer of $(Mg_4C_{60})_\infty$. Performing a bandpass-filtered inverse fast Fourier transform (iFFT) discards the lower frequencies and removes the aperiodic pixel noise. The Fourier-filtered image of the magnified area (Fig. 3e) clearly shows the hexagonal morphology of the covalently interconnected fullerenes. A closer inspection of a roughly 2-μm^2 area reveals some variations in the periodic structure of the flakes, characteristic of moiré-like superstructures (Fig. 3f). The presence of discreet peaks in the FFT (Fig. 3f, inset) indicates that the layers are single crystalline. Such variations in the periodic structure can be rationalized by considering mechanical strain resulting from ion diffusion during Mg deintercalation, which leads to local changes in the alignment of the layers with respect to each other.

To elucidate the optoelectronic properties of this material, we measured the photoluminescence (PL) of molecular C_{60}, bulk graphullerite and graphullerene bilayer. The PL spectral shape of graphullerite is significantly different from that of molecular C_{60}, particularly in the high-energy region (Fig. 4a). Furthermore, the PL peak of graphullerene bilayer is slightly blueshifted compared with that of bulk graphullerite, consistent with trends observed in other 2D materials[13]. In C_{60} crystals, the fundamental transition between the conduction band minimum and valence band maximum is parity forbidden because of the icosahedral symmetry of the molecule. Therefore, the (0,0) vibronic transition (ground vibrational levels in both S_1 and S_0 states) corresponding to the bandgap energy (about 1.9 eV) is not observed[14]. Instead, the PL spectrum consists of redshifted (0,1) and (0,2) transitions. The emergence of the higher-energy PL in graphullerite and graphullerene suggests that the covalent polymerization leads to a large change in the electronic structure near the bandgap, making the parity-forbidden (0,0) transition allowed. A more detailed analysis of the PL spectra from $(Mg_4C_{60})_\infty$ is in Extended Data Fig. 8.

Polarization-resolved PL measurements show that graphullerite exhibits polarized emission: the PL intensity depends on the analyser angle (Fig. 4a, inset), reflecting the anisotropic structure of the *b*–*c* plane. We note that the presence of counterions in the structure is detrimental to its optical properties: the PL intensity of the crystals increases by more than two orders of magnitude following Mg deintercalation.

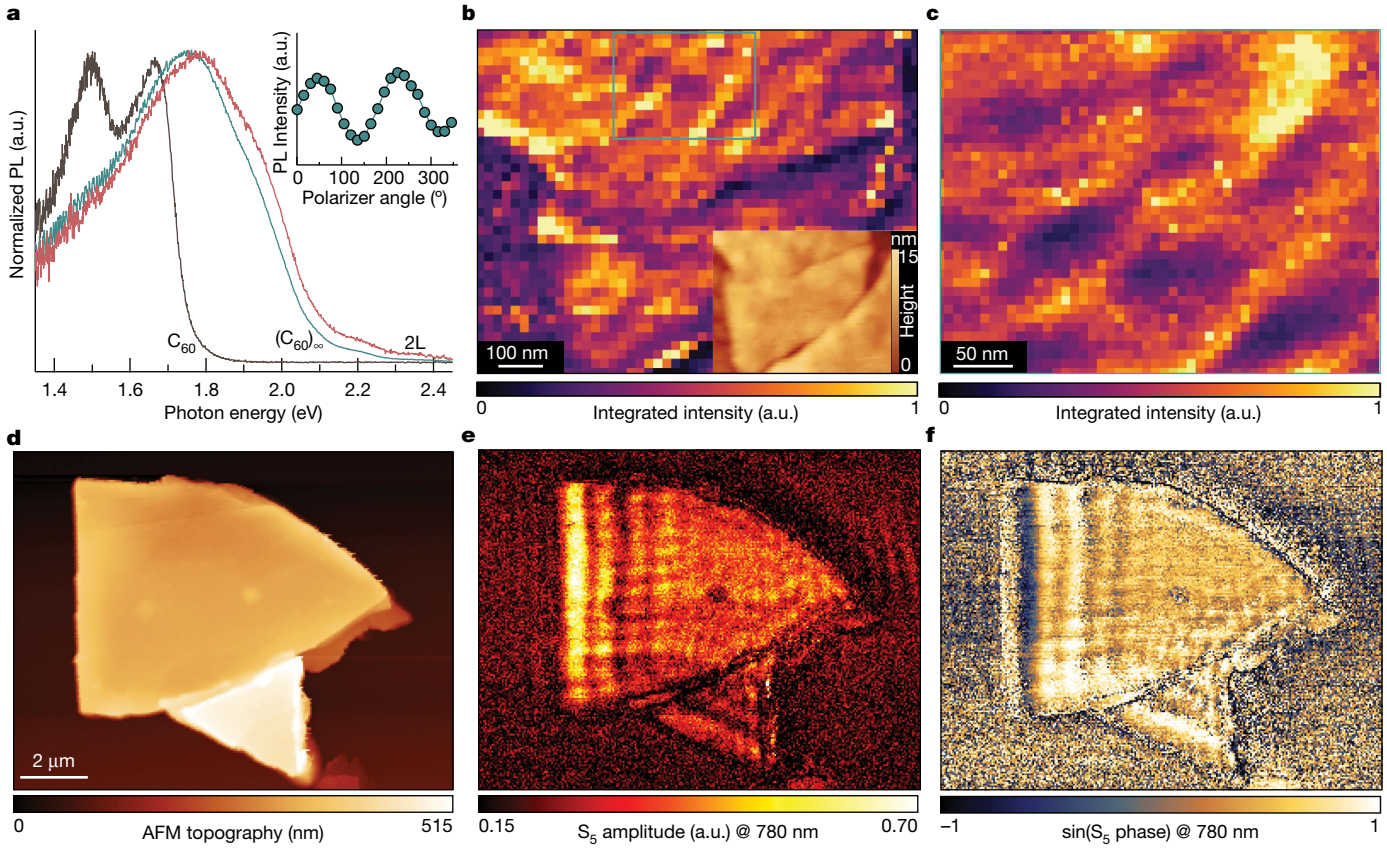

Fig. 4 | Photoluminescence and scanning near-field optical microscopy. **a**, PL spectra of molecular C_{60}, bulk graphullerite and bilayer graphullerene (2L). Inset: the emission polarization dependence of the PL intensity for graphullerite. The highest emission is presumably along the *b* axis where the fullerenes are doubly connected, and the lowest intensity between two single σ bonds, 90° with respect to the *b* axis. **b**, Nano-PL image of a 12-nm-thick graphullerene flake. At each pixel, a full PL spectrum is acquired and integrated over the entire emission range (700–900 nm). Inset: AFM topography of the flake. **c**, High-resolution image of the region defined by the blue box in **b**, showing that the PL intensity varies on the roughly 50-nm length scale. The pixel size is 8 × 8 nm^2. **d**, Topographic image of 315-nm-thick flake of graphullerite obtained using AFM. **e**, Near-field amplitude collecting at the fifth harmonic of the tip tapping frequency (S_5) of the flake shown in **d** using an incident laser wavelength of 780 nm. **f**, Sine of the associated near-field phase normalized to the SiO_2 substrate. Both near-field channels in **e** and **f** show oscillations emanating from the edge of the graphullerite flake characteristic of both waveguide and air modes.

These findings demonstrate the importance of the deintercalation process that yields a charge-neutral purely carbon-based material without counterions.

Changing the atomic registry between vdW layers through twisting or lattice mismatch can modulate the optoelectronic properties of 2D materials. In particular, moiré engineering provides a powerful approach for tailoring new excitonic systems[15]. To test whether the formation of moiré-like superstructures in graphullerene (Fig. 3f) affects the optical properties of the flakes, we performed near-field nano-photoluminescence (nano-PL) imaging[16] on a 12-nm-thick flake.

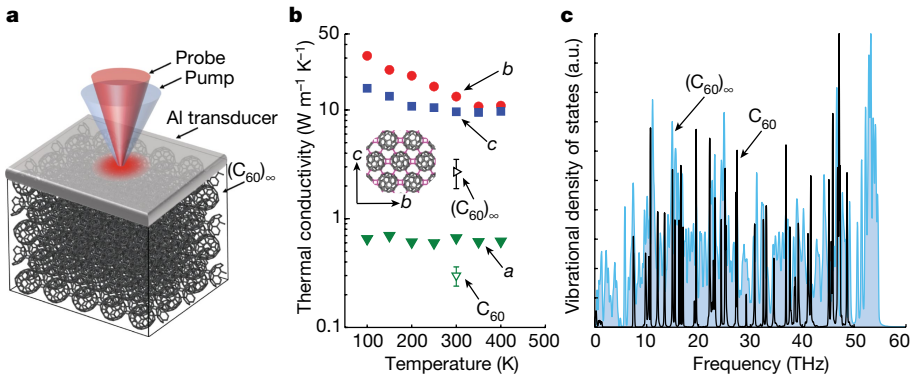

Fig. 5 | Thermal transport properties of graphullerite. **a**, Schematic of the thermal conductivity measurement. **b**, Experimentally measured thermal conductivities of a few-micrometres-thick graphullerite flake at room temperature (black open triangle) and a molecular C_{60} single crystal (green open triangle). The error bars incorporate the standard deviation between measurements and propagated uncertainty of transducer properties and the specific heat of the sample. The filled symbols represent the non-equilibrium molecular dynamics predictions for the three crystallographic directions. **c**, Vibrational density of states of molecular C_{60} and graphullerite showing additional modes throughout the vibrational spectrum for the 2D polymer phase.

We find that the lack of the long-range registry along the stacking direction, as deduced from the PXRD and HR-TEM, leads to variations in the optical response and formation of linear domains with different PL intensities (Fig. 4b,c). Although in this study we did not twist the material intentionally, these findings suggest that tuning the optoelectronic properties of graphullerene is possible by the construction of heterostructures with different twist angles.

Maps of the near-field optical response obtained using scattering-type scanning near-field optical microscopy (s-SNOM) further attest to the material quality. Figure 4d–f shows AFM and s-SNOM images with systematic oscillations in the near-field amplitude and phase (that is, near-field fringes) emanating from the edges of a thin graphullerite flake (thickness 315 nm). Such fringes in the near-field signal arise owing to interference between modes propagating in either free space near the crystal surface or within the crystal bulk (so-called air modes and waveguide modes, respectively)[17]. To observe either phenomenon, a low density of defects is required in the graphullerite flake to prevent decoherence of propagating light. Thus, the observation of near-field fringes corroborates the high quality of our crystals and suggests that it may be a viable platform for further study of 2D confined light.

Finally, we elucidate the thermal conductivity (k) of graphullerite (Fig. 5a). Vibrational thermal transport is strongly impacted by the strength of the interatomic and intermolecular interactions[18]. In fullerene-based materials, the modification of intermolecular interactions has been shown to impact the vibrational scattering mechanisms affecting k (refs. [19–22]). Figure 5b compares the room temperature k of mechanically exfoliated, thin, bulk graphullerite flakes with that of molecular C_{60} crystals. Unlike previous reports in which chemical modifications of C_{60} resulted in reductions of k (refs. [18–20,22]), the high in-plane order and the formation of intermolecular covalent bonds in graphullerite enhance thermal transport. Graphullerite shows a marked increase in k (2.7 W m^{-1} K^{-1}) that is nearly one order of magnitude higher than that measured in molecular C_{60} crystals (0.3 W m^{-1} K^{-1}). We note that this value for graphullerite is an average of all directions, as our technique is equally sensitive to thermal transport in both in-plane and cross-plane directions[23].

Molecular dynamics simulations provide fundamental insights into the vibrational thermal transport dynamics and the mechanisms that drive this order of magnitude increase in k. Figure 5b presents the molecular-dynamics-predicted k values for graphullerite along the three crystallographic directions between 100 K and 400 K. These simulations support the marked increase in k for the polymerized phase compared with that of molecular C_{60}. More specifically, the in-plane k (across the covalently bonded sheets) (Fig. 2b) is more than one order of magnitude higher than the out-of-plane k, which is similar to that of molecular C_{60} crystals. The in-plane k of graphullerene is also highly anisotropic, with the b direction (along the [2 + 2] inter-fullerene bonds) demonstrating the highest thermal transport. A comparison between the calculated vibrational spectra of C_{60} and graphullerite demonstrates that the 2D covalent bonding of C_{60} introduces many new vibrational modes throughout the spectrum (Fig. 5c). These modes provide additional pathways for heat conduction, which results in an overall increase in k for graphullerite compared with molecular C_{60}.

Fullerenes can be covalently bonded to one another by photoirradiation[24–26], solid-state reaction with alkali metals[7,27–31] and high-temperature, high-pressure annealing[32–39]. However, the resulting polycrystalline materials have high defect concentrations, mixed stoichiometries and unreacted starting materials. Moreover, the small dimensions of the single crystals obtained so far[37–39] have limited the physical and structural characterization of polyfullerenes. Although previously reported polyfullerenes[40] generally revert to molecular C_{60} when heated above 300 °C, graphullerite depolymerizes above 400 °C. Such stability results from the unique bonding architecture of graphullerite, which comprises both isolated C–C single bonds and pairs of inter-C_{60} bonds that give cyclobutane-like functionality; other polyfullerenes show only the latter type of inter-C_{60} bonding[37,38]. Perhaps the lower thermal stability of these other polyfullerenes is the result of a [2 + 2] cycloreversion, whereas the thermal stability of graphullerite is primarily due to the isolated C–C bonds.

To realize the technological promises of 2D materials, it is critical to grow macroscopic single crystals that can provide high-quality macroscopic flakes with clean surfaces. We have presented a chemical strategy to grow a 2D polymer of C_{60} as large, single crystals that are readily exfoliatable. The ability of graphullerite to withstand grinding, oxidation and treatment with acid highlights the strong in-plane covalent bonding between the fullerenes. Graphullerite vdW crystals are charge neutral and the exfoliated molecularly thin flakes have no residual counterions or impurities, providing a platform for the investigations of confined light, and the construction of quantum-materials-based devices[3,15]. This study also reveals that there is an entire family of higher- and lower-dimensional superatomic allotropes of carbon that may be chemically prepared and studied.

Online content

Any methods, additional references, Nature Research reporting summaries, source data, extended data, supplementary information, acknowledgements, peer review information; details of author contributions and competing interests; and statements of data and code availability are available at https://doi.org/10.1038/s41586-022-05401-w.

1. Hirsch, A. The era of carbon allotropes. *Nat. Mater.* **9**, 868–871 (2010).
2. Liu, X. & Hersam, M. C. Interface characterization and control of 2D materials and heterostructures. *Adv. Mater.* **30**, 1801586 (2018).
3. Andrei, E. Y. et al. The marvels of moiré materials. *Nat. Rev. Mater.* **6**, 201–206 (2021).
4. Kroto, H. W., Heath, J. R., O'Brien, S. C., Curl, R. F. & Smalley, R. E. C_{60}: buckminsterfullerene. *Nature* **318**, 162–163 (1985).
5. David, W. I. F. et al. Crystal structure and bonding of ordered C_{60}. *Nature* **353**, 147–149 (1991).
6. Novoselov, K. S. et al. Electric field effect in atomically thin carbon films. *Science* **306**, 666–669 (2004).
7. Tanaka, M. & Yamanaka, S. Vapor-phase growth and structural characterization of single crystals of magnesium doped two-dimensional fullerene polymer Mg_2C_{60}. *Cryst. Growth Des.* **18**, 3877–3882 (2018).
8. Hou, L. et al. Synthesis of a monolayer fullerene network. *Nature* **606**, 507–510 (2022).
9. Dresselhaus, M. S., Dresselhaus, G. & Eklund, P. C. *Science of Fullerenes And Carbon Nanotubes: Their Properties And Applications* (Elsevier, 1996).
10. Park, S. et al. The phototransformation of C_{60} thin films on GaAs (100) studied by in situ Raman spectroscopy. *J. Appl. Phys.* **84**, 1340–1345 (1998).
11. Burger, B., Winter, J. & Kuzmany, H. Dimer and cluster formation in C_{60} photoreaction. *Z. Phys. B* **101**, 227–233 (1996).
12. Kuzmany, H., Matus, M., Burger, B. & Winter, J. Raman scattering in C_{60} fullerenes and fullerides. *Adv. Mater.* **6**, 731–745 (1994).
13. Eda, G. et al. Photoluminescence from chemically exfoliated MoS_2. *Nano Lett.* **11**, 5111–5116 (2011).
14. Wang, Y. et al. Optical absorption and photoluminescence in pristine and photopolymerized C_{60} solid films. *Phys. Rev. B* **51**, 4547 (1995).
15. Kennes, D. M. et al. Moiré heterostructures as a condensed-matter quantum simulator. *Nat. Phys.* **17**, 155–163 (2021).
16. Darlington, T. P. et al. Imaging strain-localized excitons in nanoscale bubbles of monolayer WSe_2 at room temperature. *Nat. Nanotechnol.* **15**, 854–860 (2020).
17. Hu, D. et al. Probing optical anisotropy of nanometer-thin van der Waals microcrystals by near-field imaging. *Nat. Commun.* **8**, 1471 (2017).
18. Giri, A. & Hopkins, P. E. Spectral contributions to the thermal conductivity of C_{60} and the fullerene derivative PCBM. *J. Phys. Chem. Lett.* **8**, 2153–2157 (2017).
19. Duda, J. C., Hopkins, P. E., Shen, Y. & Gupta, M. C. Exceptionally low thermal conductivities of films of the fullerene derivative PCBM. *Phys. Rev. Lett.* **110**, 015902 (2013).
20. Giri, A. et al. Molecular tail chemistry controls thermal transport in fullerene films. *Phys. Rev. Mater.* **4**, 065404 (2020).
21. Ong, W.-L. et al. Orientational order controls crystalline and amorphous thermal transport in superatomic crystals. *Nat. Mater.* **16**, 83–88 (2017).
22. Wang, X., Liman, C. D., Treat, N. D., Chabinyc, M. L. & Cahill, D. G. Ultralow thermal conductivity of fullerene derivatives. *Phys. Rev. B* **88**, 075310 (2013).
23. Braun, J. L., Olson, D. H., Gaskins, J. T. & Hopkins, P. E. A steady-state thermoreflectance method to measure thermal conductivity. *Rev. Sci. Instrum.* **90**, 024905 (2019).
24. Rao, A. et al. Photoinduced polymerization of solid C_{60} films. *Science* **259**, 955–957 (1993).
25. Lee, K. et al. Two-dimensional fullerene assembly from an exfoliated van der Waals template. *Angew. Chem. Int. Edn* **130**, 6233–6237 (2018).
26. Okada, S. et al. Direct microscopic analysis of individual C_{60} dimerization events: kinetics and mechanisms. *J. Am. Chem. Soc.* **139**, 18281–18287 (2017).
27. Pekker, S. et al. Single-crystalline $(KC_{60})_n$: a conducting linear alkali fulleride polymer. *Science* **265**, 1077–1078 (1994).

28. Oszlányi, G., Baumgartner, G., Faigel, G. & Forró, L. Na_4C_{60}: an alkali intercalated two-dimensional polymer. *Phys. Rev. Lett.* **78**, 4438 (1997).
29. Margadonna, S. et al. Li_4C_{60}: a polymeric fulleride with a two-dimensional architecture and mixed interfullerene bonding motifs. *J. Am. Chem. Soc.* **126**, 15032–15033 (2004).
30. Riccò, M. et al. Unusual polymerization in the Li_4C_{60} fulleride. *Phys. Rev. B* **72**, 155437 (2005).
31. Heguri, S. & Kobayashi, M. The absence of a metallic phase in magnesium fullerides Mg_xC_{60} ($1<x\leq6$). *Solid State Commun.* **150**, 1489–1492 (2010).
32. Iwasa, Y. et al. New phases of C_{60} synthesized at high pressure. *Science* **264**, 1570–1572 (1994).
33. Nunez-Regueiro, M., Marques, L., Hodeau, J.-L., Béthoux, O. & Perroux, M. Polymerized fullerite structures. *Phys. Rev. Lett.* **74**, 278–281 (1995).
34. Sundqvist, B. Fullerenes under high pressures. *Adv. Phys.* **48**, 1–134 (1999).
35. Moret, R., Launois, P., Persson, P.-A. & Sundqvist, B. First X-ray diffraction analysis of pressure polymerized C_{60} single crystals. *Europhys. Lett.* **40**, 55 (1997).
36. Davydov, V. et al. Tetragonal polymerized phase of C_{60}. *Phys. Rev. B* **58**, 14786 (1998).
37. Chen, X. & Yamanaka, S. Single-crystal X-ray structural refinement of the 'tetragonal' C_{60} polymer. *Chem. Phys. Lett.* **360**, 501–508 (2002).
38. Chen, X., Yamanaka, S., Sako, K., Inoue, Y. & Yasukawa, M. First single-crystal X-ray structural refinement of the rhombohedral C_{60} polymer. *Chem. Phys. Lett.* **356**, 291–297 (2002).
39. Yamanaka, S. et al. Electron conductive three-dimensional polymer of cuboidal C_{60}. *Phys. Rev. Lett.* **96**, 076602 (2006).
40. Iwasa, Y. et al. Pressure-induced cross-linking of C_{60}. *Synth. Met.* **70**, 1407–1408 (1995).

Methods

Synthesis

Single crystals of $(Mg_4C_{60})_\infty$ were grown by the CVT technique. C_{60} (MTR, 99.9%, sublimed) and Mg powder (Sigma-Aldrich, 50 mesh, ≥99%) were combined in a Mg:C_{60} 6:1 molar ratio, ground into a homogeneous mixture, pressed into a pellet and placed in a quartz tube (7-mm inner diameter) in a nitrogen-filled glovebox. The tube was then sealed under vacuum and placed in a two-zone horizontal furnace with a temperature gradient of 500 °C to 600 °C for 24 h and then allowed to cool to room temperature. Highly air-sensitive polyfulleride crystals up to a few hundred micrometres in size grew at the cold end of the tube. Selected crystal structure data are presented in Extended Data Table 1. We determined the Mg:C_{60} ratio by both SCXRD and EDS and found that the Mg:C_{60} atomic ratio varies between 3.6 and 4.4 for different crystals from the same growth batch. The lattice structure is the same for crystals within this composition range.

We note that using finer Mg powder (Alfa Aesar, 325 mesh, 99.8%) without changing the other growth conditions, we obtain $(Mg_2C_{60})_\infty$ crystals, similar to ref. [7].

Single crystals of pure C_{60} were grown using a similar procedure but without added Mg powder. The crystal structure is as reported[5].

Optical microscopy

Optical microscope images were taken on a Nikon ECLIPSE LV150N microscope.

Single-crystal X-ray determination

SCXRD data were collected using an Agilent SuperNova X-ray diffractometer configured in a four-circle kappa goniometer geometry and a mirror-monochromated microfocus Cu Kα radiation(1.54184 Å). Single crystals were mounted on a 150-µm MiTeGen MicroMount pin using Paratone N oil and cooled to 100 K with an Oxford Cryosystems nitrogen flow apparatus. X-ray intensities were measured with the Titan charge-coupled-device (CCD) detector placed about 34–42 mm from the sample. The data were processed with CrysAlisPro[41] (Oxford) and corrected for absorption. The structures were determined in OLEX2 version 1.5[42] using SHELXT[43] and refined using SHELXL[44]. Two of the Mg atoms were found to be disordered and modelled as occupying three possible positions each.

Device fabrication and electronic transport measurements

$(Mg_4C_{60})_\infty$ crystals were mechanically exfoliated in a nitrogen-filled glovebox with oxygen and water levels <0.1 ppm, using Scotch-brand magic tape. The 285-nm silicon dioxide (SiO_2)/silicon (Si) substrates (p doped) were cleaned with a low-power oxygen plasma etch for 5 min before transfer and heated to 100 °C for 2 min for the transfer process. Flakes of desired thicknesses were identified by optical contrast and transferred to the pre-cleaned 285-nm SiO_2/Si substrates via a dry-transfer method; a cold polydimethylsiloxane (PDMS) stamp (−100 °C) was used to pick up and subsequently release the flakes on the designated spot at a higher temperature (−20 °C). A high-resolution stencil mask technique was used to fabricate rigorously air-free devices inside the glovebox. This process is free of solvents and polymers and helps to preserve the quality of the crystals, eliminating possible artefacts that might arise from conventional lithography processes using solvent-based methods and conducting paints usually applied as contacts for bulk crystals. Stencil masks were fabricated from silicon nitride (Si_3N_4)(500 nm)/Si(300 µm)/Si_3N_4(500 nm) wafers. At first, a combination of photolithography, reactive ion etching, and wet etching (potassium hydroxide solution) was used to create 200-µm and 500-µm square windows of Si_3N_4. Subsequently, the desired patterns of devices were written with photolithography on the windows. In the last step, we used reactive ion etching to remove Si_3N_4 in the exposed patterned area. We used a micro-positioner to align and place the prefabricated Si_3N_4 masks on transferred flakes. A small amount of vacuum grease (Apiezon H) was used to secure the mask onto the substrate. The device fabrication was completed by evaporating gold (Au) metal as electrical contacts. The final device was cut, mounted on a 16-pin chip carrier and wire-bonded inside the glovebox. Finally, the chip carrier was covered with glass and loaded into the cryostat for the measurements. Electronic transport measurements were performed in a Quantum Design Physical Property Measurement System. Electrical conductivity was measured with a combination of a Keithley 2400 source meter and an Agilent 34401A Digital Multimeter with a high internal impedance of more than 10 GΩ.

Deintercalation

$(Mg_4C_{60})_\infty$ crystals were immersed in a 10% v/v aqueous solution of hydrochloric acid, acetic acid or nitric acid for 2 h. The supernatant was decanted, the crystals were rinsed thoroughly with deionized water and acetone, and dried in vacuo at room temperature. The Mg:C_{60} ratio was determined by EDS. Hydrochloric acid only partially removed the Mg to give $(Mg_3C_{60})_\infty$, whereas suspending $(Mg_4C_{60})_\infty$ in dilute aqueous solutions of acetic acid or nitric acid decreased the Mg:C_{60} ratio to 0.5:1. Our hypothesis is that these chelating acids form Mg salts that are more easily removed from the structure than those produced with hydrochloric acid. To remove the remaining Mg from the crystals, we suspended $(Mg_{0.5}C_{60})_\infty$ in *N*-methylpyrrolidone at 180 °C for 12 h. The supernatant was then decanted, the crystals were rinsed thoroughly with tetrahydrofuran and dried in vacuo at 80 °C for 12 h.

Powder X-ray diffraction

The crystals were ground and loaded on a zero-background Si sample holder. PXRD data were collected on a PANanlytical Aeris diffractometer housed in a glovebox. The PXRD pattern of graphullerite features two broad peaks at 9.3° and 19° (Extended Data Fig. 2). We assign these peaks to the (200) and (400) reflections based on a model constructed from the SCXRD structure of $(Mg_4C_{60})_\infty$, assuming preferred orientation with the basal plane parallel to the substrate (marked as red vertical lines in Extended Data Fig. 2). Such a preferred orientation is common for vdW materials. When compared with $(Mg_4C_{60})_\infty$, the (200) and (400) peaks of graphullerite are shifted to lower angles, suggesting that the diffusion of ions during deintercalation results in an expansion along the *a* axis—the stacking direction. The peak broadening is due to stacking faults and inhomogeneous strain as a result of ion diffusion during deintercalation[45].

Scanning electron microscopy and energy-dispersive X-ray spectroscopy

SEM samples were prepared by placing single crystals on carbon tape. Scanning electron micrographs were collected using a ZEISS Sigma VP SEM. EDS was performed with a Bruker XFlash 6 | 30 attachment.

Mechanical exfoliation

Graphullerite crystals were mechanically exfoliated using Scotch-brand magic tape. The 285-nm SiO_2/Si substrates (p doped) were cleaned with a low-power oxygen plasma etch for 5 min before transfer and heated to 100 °C for 2 min for the transfer process. Flakes of desired thicknesses were identified by optical contrast using an optical microscope.

Atomic force microscopy

AFM images were acquired in PeakForce QNM in scanning mode using a Bruker Dimension FastScan AFM under ambient conditions. Height profiles were analysed and extracted from the AFM images using Gwyddion software.

Raman spectroscopy

Raman measurements were performed on $(Mg_4C_{60})_\infty$ and graphullerite, as well as on bilayer graphullerene prepared by mechanical exfoliation. The samples were sealed in a 1-cm cuvette inside a nitrogen-filled

glovebox with oxygen and water levels less than 0.1 ppm and then placed on a home-built micro-Raman spectrometer. Light from a solid-state laser with wavelength λ = 532 nm reflects off a dichroic beamsplitter in a Nikon Eclipse Ti/U inverted microscope and is focused by a ×40, 0.6-numerical-aperture (NA) objective to an approximately 1-μm^2 spot on the sample. The backscattered light was collected by the same objective and passes through a 50-μm confocal pinhole before entering a 0.3-m Acton spectrometer where a 1,200 g mm^{-1} diffraction grating disperses it onto a PIXIS 400 CCD imaging detector. Typical laser powers were between 20 μW and 100 μW. Spectra were measured on at least two different exfoliated crystals for a particular sample, and in each case, two consecutive spectra were measured on the same spot with a 300-s exposure time to check for sample degradation. The spectral resolution is typically 3.7 cm^{-1} and was determined using the λ = 546 nm peak of a mercury calibration lamp.

High-resolution transmission electron microscopy

Graphullerite crystals were mechanically exfoliated using Scotch-brand magic tape, and transferred to a 200-mesh copper PELCO TEM grid with carbon support film using a PDMS stamp under ambient conditions. HR-TEM was performed on FEI Talos F200X. We determined the average centroid-to-centroid distance between neighbouring C_{60} units (8.8 ± 0.3 Å) by applying an FFT to the TEM image (Fig. 3f, inset). This value is in good agreement with the corresponding distance within a molecular plane of $(Mg_4C_{60})_\infty$, as calculated from the SCXRD data (9.16 Å).

Photoluminescence spectroscopy

PL measurements were performed on single crystals of molecular C_{60} and graphullerite, as well as on graphullerene bilayer prepared by mechanical exfoliation. The C_{60} crystals were glued to BK7 glass substrates using silver paste plus (SPI Supplies). A continuous-wave laser (λ = 450 nm) was used as an excitation light source. The laser was sent to a ×40 microscope objective and focused onto a sample in a cryostat. The PL was collected with the same objective. The PL spectrum was recorded using a liquid-nitrogen-cooled CCD equipped with a monochromator. Long-pass filters were used to cut the scattering of the excitation laser. The emission polarization dependence was measured by placing a linear polarizer in the detection path and rotating it. The sensitivity of the set-up and its polarization dependence owing to the rotation of the linear polarizer was calibrated using a standard white light. The PL spectra reported in this paper were taken under vacuum at room temperature.

We observed a multiple-peak structure in the PL spectrum of $(Mg_4C_{60})_\infty$ (Extended Data Fig. 8a). We also confirmed that the PL intensity increases linearly with increasing excitation laser power (Extended Data Fig. 8b). The observed spectral shape suggests that the optical transition in $(Mg_4C_{60})_\infty$ is dominated by a strong vibronic nature, where the electronic exciton transition and the vibration are coupled to each other. Indeed, the multiple-peak structure is found to be well explained by considering the single-oscillator Franck–Condon model[46]. We performed the theoretical fitting according to the Franck–Condon analysis (equations (3) and (4) in ref. [46]), where the PL spectral shape is described by the vibronic (0,0) transition energy E_0, the frequency of the vibration involved ω (corresponding energy is $\hbar\omega$, where $\hbar$ is the reduced Planck constant), the Huang–Rhys factor S and the width of the vibronic transition w. The refractive index is assumed to be constant. The fitting result, shown with the solid line in Extended Data Fig. 8a, explains the experimental spectral shape. For this Franck–Condon analysis, we used the vibrational frequency $\hbar\omega$ = 1,429 cm^{-1} (177 meV) because this T_{1u} mode is known to give rise to the most intense vibronic PL sideband in C_{60}-based materials[14]; one can see the equally spaced PL peaks in Extended Data Fig. 8a, whose space is $\hbar\omega$ = 1,429 cm^{-1}. The obtained Huang–Rhys factor of 2.7 indicates a strong coupling between the excitonic transition and the vibrational mode. The fitting also yielded the values E_0 = 2.02 eV and w = 0.166 eV (full-width at half-maximum). The fact that the PL of $(Mg_4C_{60})_\infty$ is described by the Franck–Condon model suggests a large change in the electronic states near the bandgap compared with those of pristine C_{60} crystals. In the pristine C_{60} crystals, the fundamental transition between the conduction band minimum and valence band maximum is parity forbidden, thus the vibronic (0,0) transition is not observed and accordingly the Franck–Condon model is not applicable (Fig. 4a). The PL results suggest that the covalent polymerization leads to a large change in the electronic structure near the bandgap, making the parity-forbidden (0,0) transition allowed.

Near-field nano-photoluminescence imaging

Graphullerite crystals were mechanically exfoliated onto a 70-nm Au/SiO_2/Si substrate and heated to 100 °C for 2 min for the transfer process. Imaging of the nano-PL is performed at room temperature on the TRIOS near-field optical microscope from Horiba Scientific. A single-mode helium–neon laser (633 nm) is focused from the side onto the apex of an Au-coated AFM probe (OMNI-TERS-Au, AppNano) with a ×100, 0.7-NA long-working-distance objective (Mitutoyo). This excites a localized plasmon that enhances the local optical field, with a spatial extent of about 10 nm. The enhanced PL is collected through the same objective and passed to the LabRAM HR Evolution spectrometer (Horiba Scientific), and recorded with an electron multiplying CCD (Synapse II, Horiba Scientific). Hyperspectral imaging is conducted in 'Spec-Top' mode with 'dual-spec' used, a hybrid contact/non-contact scanning mode where the nano-PL is measured with the probe in contact with the sample, then retracted about 20 nm to measure the far-field background and move to next pixel, avoiding contact wear of the probe and sample. Excitation powers for the nano-PL images were 200 μW with exposure times of 150 ms.

Scattering-type scanning near-field optical microscopy

s-SNOM measurements were conducted using a commercial Neaspec system under ambient conditions using Arrow AFM probes with a nominal resonant frequency of f = 75 kHz. The sample was illuminated with a tunable continuous-wave laser from M-squared (titanium–sapphire module with an output range of 700–1,000 nm (SolsTiS)). The backscattered light was registered by pseudo-heterodyne interferometry and demodulated at the fifth harmonic of the tip tapping frequency to suppress background contribution to the detected signal.

Thermal conductivity measurements

We used two different pump–probe thermoreflectance techniques to measure the thermal conductivities of C_{60} and graphullerite. For the C_{60} crystals, we measured the thermal conductivity with time-domain thermoreflectance (TDTR), a pump–probe experiment that utilizes sub-picosecond laser pulses to monitor the transient changes in reflectivity on the sample surface owing to changes in temperature induced from the pump pulses. In our measurements, we utilized TDTR in a two-tint configuration, described elsewhere[47]. Before TDTR measurements, we coated the surface of the samples with 80 nm of aluminium (Al) via electron-beam evaporation. We used an optical camera to focus the pump and probe spots on the surface of each isolated crystal that we test. At focus, the pump and probe 1/e^2 diameters were 4.5 μm and 4.5 μm, respectively. To measure thermal conductivity, we modulated the pump path at 8.4 MHz, and monitored the changes in reflectivity from the reflected probe pulses owing to temperature changes induced from the modulated pump heating event as a function of pump–probe delay time (Extended Data Fig. 9a). We monitored the negative ratio of the in-phase to out-of-phase voltages recorded from the lock-in amplifier and fit this signal to the solution to the cylindrical heat equation for an 80-nm Al film on a semi-infinite C_{60} substrate[48]. The high-frequency modulation and spot sizes ensure that this semi-infinite assumption is valid[49]. For our analysis, we assumed volumetric heat capacities for the Al and C_{60} from previous literature, and a thermal conductivity for the Al film of 180 W m^{-1} K^{-1} as determined via the Wiedemann–Franz

law applied to four-point probe resistivity measurements, and we set the Al/C_{60} thermal boundary conductance to 100 MW m^{-2} K^{-1}, leaving the only free parameter in our TDTR fit as the thermal conductivity of C_{60}. We have negligible sensitivity to the Al/C_{60} thermal boundary conductance owing to the low thermal conductivity of the C_{60}, so our assumption for this value does not impact our results.

For graphullerite, we attempted TDTR measurements, but we were unable to obtain reliable and repeatable results owing to sample-to-sample variation and non-temperature related variations in our measured signals that arose during measurements. A major limitation in applying TDTR to graphullerite is that these crystals had a much smaller measurable cross-sectional dimension than the C_{60} crystals (for example, most graphullerite samples were only a few micrometres in measurable surface area). This limited dimensionality restricted the number of individual crystals in which we could perform reliable TDTR tests. In addition, as our TDTR spot sizes were on the order of the dimension of the sample, we observed artefacts in our measured data that could be attributed to thermoelastic effects from the pump-induced pressure wave interacting with the sample dimensions[50]. Therefore, to alleviate these measurement issues, we use steady-state thermoreflectance (SSTR)[23] to measure the thermal conductivity of the graphullerite crystals.

Similar to TDTR, SSTR is a pump–probe technique but SSTR utilizes continuous-wave lasers to measure the change in reflectivity on the surface of the sample as a function of change in pump power (Extended Data Fig. 9a). We modulate the pump beam at a low frequency (in our case, 1,000 Hz) to ensure that the temperature gradients induced during pump heating reach steady state, and we measure this thermoreflectance during steady state, as recorded from the in-phase lock-in voltage, as a function of pump power. Given that the sample has reached steady-state conditions, the temperature response is directly related to the change in heat flux from the pump path via the cylindrically symmetric Fourier law, as detailed previously[23,51]. In our specific case, SSTR offers an advantage to measuring the thermal conductivity of graphullerite as we can focus on small spot sizes (1.8 mm and 1.4 mm $1/e^2$ diameters for pump and probe, respectively), ensuring we are taking measurements in the middle of the crystals that normally we either could not measure or posed difficulty measuring with TDTR. In addition, as SSTR operates in the steady-state regime, we do not require an assumption of the heat capacity of the materials in our thermal model; given that graphullerite is a new crystal with an unknown heat capacity, this reduces our uncertainty in our determined thermal conductivity. Finally, our measurements are not subjected to the same strong thermoelastic conditions that we potentially observed when applying TDTR to these systems as the absorbed power density on the surface of the Al-coated graphullerite from the continuous-wave pump is orders of magnitude smaller than that from a short pulse with similar average power, and thus the thermally induced acoustic waves generated from the short pulse in TDTR that we posit could be impacting our measurements on these areal-confined samples are non-existent in SSTR.

We note that we also attempted SSTR measurements on the C_{60} sample that we measured with TDTR; however, owing to the much lower thermal conductivity of C_{60} compared with the graphullerene (0.3 W m^{-1} K^{-1} for C_{60} compared with 2.7 W m^{-1} K^{-1} for graphullerite), our SSTR measurements were much more sensitive to the thermal conductivity of the Al film compared with the C_{60}. Given the ninefold increase in thermal conductivity of graphullerite compared with C_{60}, the graphullerite SSTR measurements did not suffer from this same issue and were quite robust for measurements of the thermal conductivity of the relatively smaller crystallites.

Non-equilibrium molecular dynamics simulations

We performed non-equilibrium molecular dynamics (NEMD) simulations to predict the thermal conductivity of graphullerite described via the polymer consistent force-field (PCFF)[52]. The Large-scale Atomic/Molecular Massively Parallel Simulator (LAMMPS) package was used to perform all simulations[53]. Throughout the simulations, a timestep of 0.5 fs was used. For the NEMD method, we established hot and cold baths at opposite ends of the computational domain that were extended along the heat flux direction. An equal amount of heat was added and subtracted from the hot and cold sides, respectively. The equations of motion of the atoms between the baths were integrated under the microcanonical ensemble (with the number of atoms, volume and energy held constant). A steady-state temperature gradient was established across the computational domain, which is averaged over 9 ns. As size effects can considerably reduce the NEMD-predicted thermal conductivity owing to scattering of longer wavelength vibrations at the walls and the baths along the heat flux direction, we performed simulations on multiple domain lengths. From these simulation results, the inverse of thermal conductivity ($1/k$) was compared with the inverse of the length of the simulation domain length ($1/d$) and a linear extrapolation to $1/d \rightarrow 0$ corresponds to $1/k_{\infty}$, the inverse of which is the approximate thermal conductivity of the bulk structure[54] (Extended Data Fig. 9b).

Differential scanning calorimetry

DSC traces were collected on a DSC Q2000 (TA Instruments) equipped with an RCS90 cooling accessory. Baseline calibration was performed with sapphire disks. The temperature and the cell constant were calibrated using an indium standard.

Thermogravimetric analysis

TGA traces were collected on a TGA Q500 (TA Instruments) under N_2 flow.

Zeta-potential analysis

The zeta potential of graphullerite was measured using a Malvern nano-ZS zeta-potential analyser. Microcrystalline crystals were suspended in isopropanol by sonication in an ultrasonic bath (fisherbrand CPX2800) for 1 h and then centrifuged for 15 min at 5,000 r.p.m. to separate the sediment from the colloidal suspension.

Data availability

The data that support the findings of this study are present in the paper and its Extended Data. The crystallographic data presented in this work are available through the Cambridge Crystallographic Data Centre (CCDC) referencing deposition no. 2151576. Further data are available from the corresponding authors upon reasonable request.

41. CrysAlis PRO (Agilent Technologies Ltd, Yarnton, Oxfordshire, UK, 2014).
42. Dolomanov, O. V., Bourhis, L. J., Gildea, R. J., Howard, J. A. K. & Puschmann, H. OLEX2: a complete structure solution, refinement and analysis program. *J. Appl. Crystallogr.* **42**, 339–341 (2009).
43. Sheldrick, G. M. SHELXT—integrated space-group and crystal-structure determination. *Acta Crystallogr. A* **71**, 3–8 (2015).
44. Sheldrick, G. M. Crystal structure refinement with SHELXL. *Acta Crystallogr. C* **71**, 3–8 (2015).
45. Holder, C. F. & Schaak, R. E. Tutorial on powder X-ray diffraction for characterizing nanoscale materials. *ACS Nano* **13**, 7359–7365 (2019).
46. Ho, P. K., Kim, J.-S., Tessler, N. & Friend, R. H. Photoluminescence of poly(*p*-phenylenevinylene)–silica nanocomposites: evidence for dual emission by Franck–Condon analysis. *Chem. Phys.* **115**, 2709–2720 (2001).
47. Kang, K., Koh, Y. K., Chiritescu, C., Zheng, X. & Cahill, D. G. Two-tint pump–probe measurements using a femtosecond laser oscillator and sharp-edged optical filters. *Rev. Sci. Instrum.* **79**, 114901 (2008).
48. Cahill, D. G. Analysis of heat flow in layered structures for time-domain thermoreflectance. *Rev. Sci. Instrum.* **75**, 5119–5122 (2004).
49. Braun, J. L. & Hopkins, P. E. Upper limit to the thermal penetration depth during modulated heating of multilayer thin films with pulsed and continuous wave lasers: a numerical study. *J. Appl. Phys.* **121**, 175107 (2017).
50. Wang, X., Ho, V., Segalman, R. A. & Cahill, D. G. Thermal conductivity of high-modulus polymer fibers. *Macromolecules* **46**, 4937–4943 (2013).
51. Braun, J. L., Szwejkowski, C. J., Giri, A. & Hopkins, P. E. On the steady-state temperature rise during laser heating of multilayer thin films in optical pump–probe techniques. *J. Heat Transfer* **140**, 052801 (2018).

52. Sun, H. COMPASS: an ab initio force-field optimized for condensed-phase applications—overview with details on alkane and benzene compounds. *J. Phys. Chem. B* **102**, 7338–7364 (1998).
53. Plimpton, S. Fast parallel algorithms for short-range molecular dynamics. *J. Comput. Phys.* **117**, 1–19 (1995).
54. Schelling, P. K., Phillpot, S. R. & Keblinski, P. Comparison of atomic-level simulation methods for computing thermal conductivity. *Phys. Rev. B* **65**, 144306 (2002).

Acknowledgements This work was primarily funded by the Columbia MRSEC on Precision-Assembled Quantum Materials (PAQM) under award number DMR-2011738, and the Air Force Office of Scientific Research under grant FA9550-22-1-0389. Surface characterization of graphullerene was supported by the NSF CAREER award DMR-1751949 (X.R.). Calorimetry measurements were supported by the NSF award CBET-2017198 (X.R.). C.N. acknowledges support from the Office of Naval Research Award N00014-20-1-2477, and thanks S. Buckler and D. Buckler for their generous support. M.M., C.J.D., A.G. and P.E.H. acknowledge support from the Office of Naval Research, grant numbers N00014-20-1-2686 and N00014-21-1-2622. Infrared nano-imaging experiments are supported under Energy Frontier Research Center on Programmable Quantum Materials funded by the US Department of Energy (DOE), Office of Science, Basic Energy Sciences (BES), under award DE-SC0019443. E.M. was supported in part by the Yad Hanadiv and Weizmann Women in Science Award for postdoctoral fellowship support. A.M.E. was supported by the Schmidt Science Fellows, in partnership with the Rhodes Trust. M.R and P.K. were supported by Army Research Office under Award W911NF-18-1-0366. R.A.W. and A.K.B. were supported by Arnold O. Beckman Fellowships in Chemical Sciences. T.H. acknowledges the postdoctoral fellowship support of JSPS Overseas Research Fellowships. X-ray diffraction, electron microscopy, AFM, zeta-potential and TGA measurements were performed in the Shared Materials Characterization Laboratory at Columbia University. We thank L. M. Campos and E. M. Churchill for their assistance with the DSC measurements. Raman spectroscopy measurements were supported by the Barnard College Department of Chemistry and Office of the Provost. We thank N. Cislo for assistance with early Raman spectroscopy measurements.

Author contributions Conceptualization: E.M., J.Y., M.L.S., C.N., X.R. Methodology and investigation: E.M., A.M.E., S.T.B., A.K.B., R.A.W. Electron microscopy: A.M.E., A.Z. Device fabrication and electrical transport: M.Rezaee., P.K. Photoluminescence: T.H., X.Z., T.P.D, N.F.-M., P.J.S. s-SNOM: D.J.R., D.N.B. Raman spectroscopy: M.Reza., A.C.C. Thermal properties: M.M., C.J.D., A.G., P.E.H. Writing: E.M., A.M.E., M.L.S., C.N., X.R. Supervision: M.L.S., C.N., X.R.

Competing interests The authors declare no competing interests.

Additional information

Supplementary information The online version contains supplementary material available at https://doi.org/10.1038/s41586-022-05401-w.

Correspondence and requests for materials should be addressed to Elena Meirzadeh, Michael L. Steigerwald, Jingjing Yang, Colin Nuckolls or Xavier Roy.

Peer review information *Nature* thanks Andreas Hirsch and the other, anonymous, reviewer(s) for their contribution to the peer review of this work.

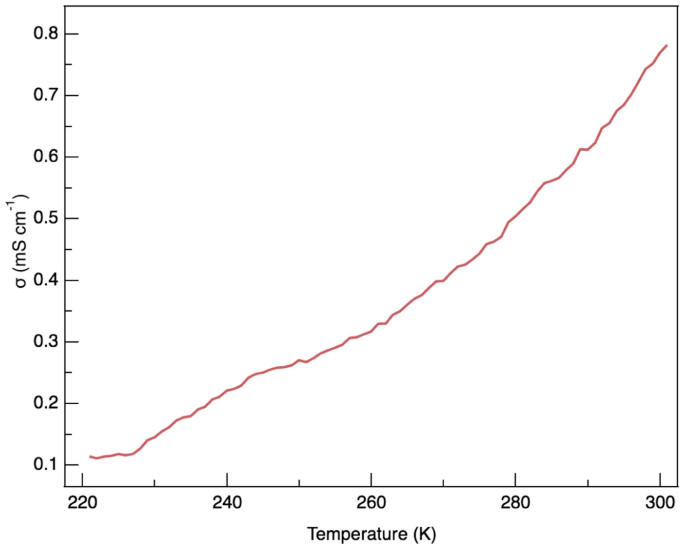

Extended Data Fig. 1 | Electrical transport properties of $(Mg_4C_{60})_\infty$. Electrical conductivity (σ) of $(Mg_4C_{60})_\infty$ versus temperature.

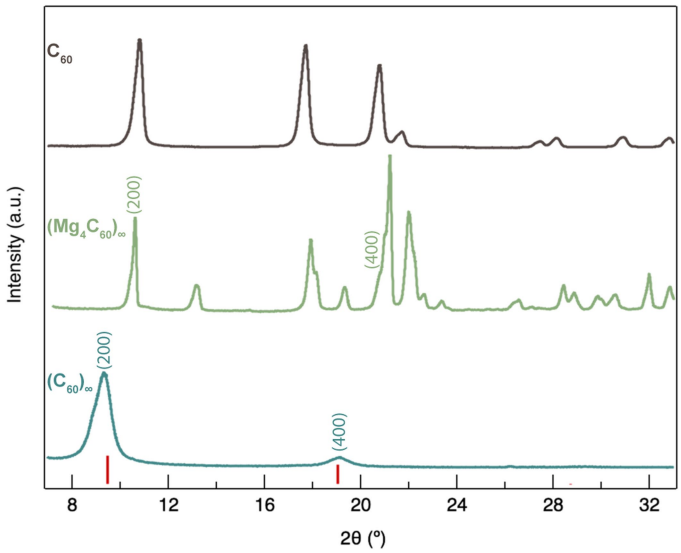

Extended Data Fig. 2 | Powder X-ray diffraction of C_{60} polymers. PXRD pattern of graphullerite $(C_{60})_\infty$, $(Mg_4C_{60})_\infty$, and molecular C_{60}. The red vertical lines represent the calculated peak positions for $(Mg_4C_{60})_\infty$, assuming a preferred orientation and 1.8 Å expansion along the *a* axis, the stacking direction.

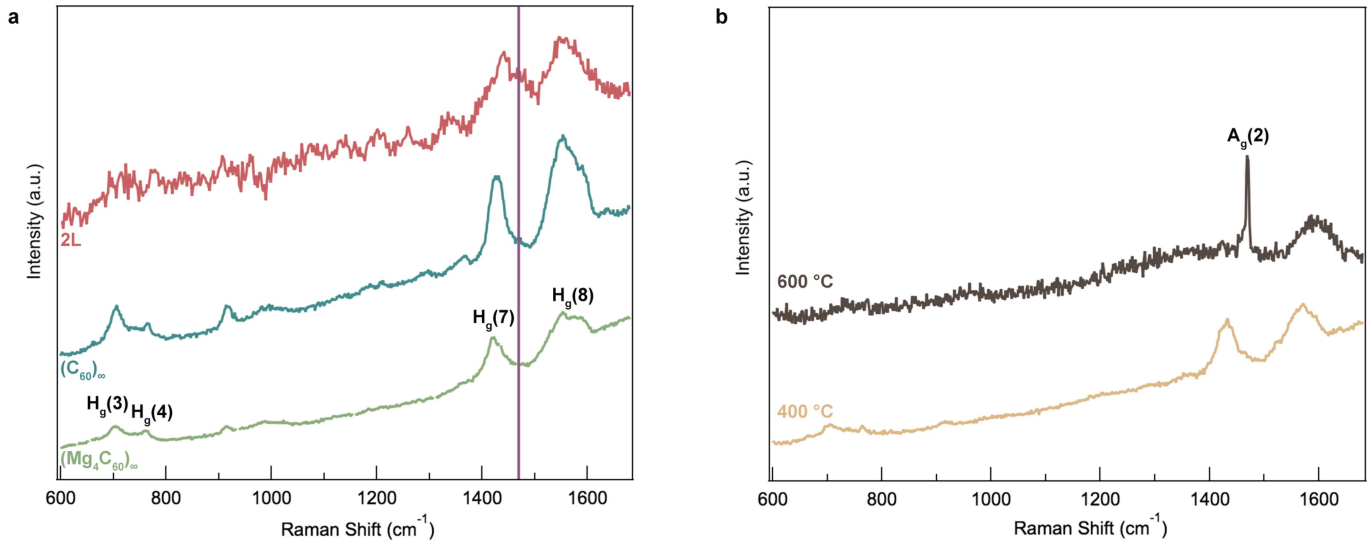

Extended Data Fig. 3 | Raman spectra and thermal stability of C_{60} polymers. **a**, Raman spectra of $(Mg_4C_{60})_\infty$, graphullerite $(C_{60})_\infty$, and mechanically exfoliated bilayer graphullerene (2L). The purple vertical line denotes the pentagonal pinch mode for molecular C_{60} (1,469 cm^{-1}). The $A_g(2)$ mode of graphullerite and graphullerene may overlap with the broad $H_g(7)$ mode at 1,420 cm^{-1}. **b**, Raman spectra of graphullerite after annealing at 400 and 600 °C for 1 h. The $A_g(2)$ mode characteristic of molecular C_{60} appears at 1,469 cm^{-1} after annealing at 600 °C.

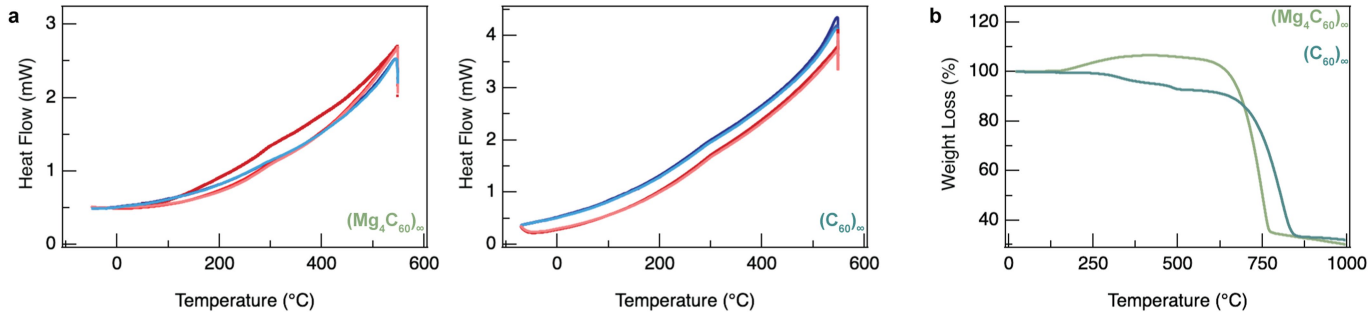

Extended Data Fig. 4 | Calorimetry and thermogravimetric analysis of C_{60} polymers. a, DSC traces of $(Mg_4C_{60})_\infty$ and graphullerite crystals. The heat flow was measured as a function of temperature at a constant temperature ramp of 10 °C min^{-1} during heating and 5 °C min^{-1} during cooling with a 50 ml /min^{-1} nitrogen cell purge flow. **b**, Weight loss as a function of temperature for molecular C_{60} and $(Mg_4C_{60})_\infty$ under N_2 at a constant temperature ramp of 10 °C min^{-1}, measured by TGA. The 6% increase in the $(Mg_4C_{60})_\infty$ data is presumably due to the formation of MgO.

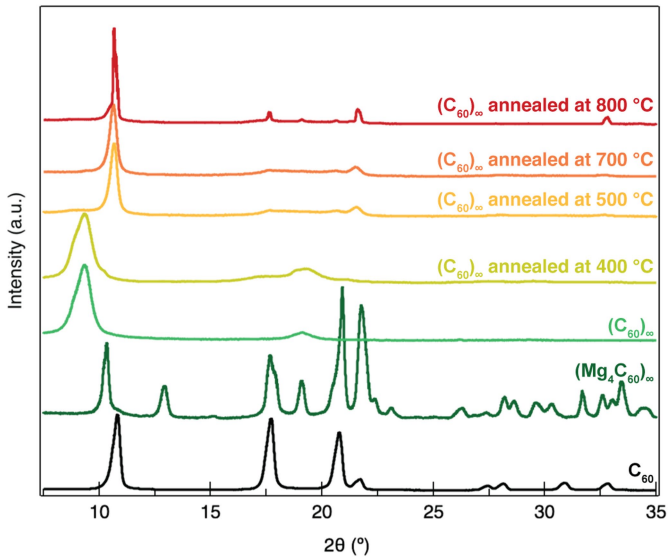

Extended Data Fig. 5 | Powder X-ray diffraction of graphullerite after thermal treatment. The PXRD patterns of graphullerite after annealing *in vacuo* for 1 h at different temperatures, along with the patterns of $(Mg_4C_{60})_\infty$ and molecular C_{60}. Above 500 °C the covalently bonded sheets depolymerize, and molecular C_{60} peaks emerge and become more intense above 800 °C.

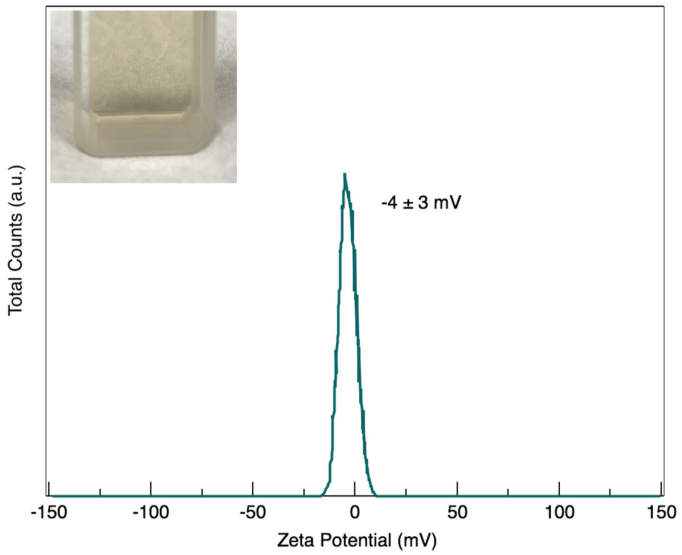

Extended Data Fig. 6 | Zeta potential of graphullerite suspended in isopropanol. Inset: image of the suspension used for this measurement.

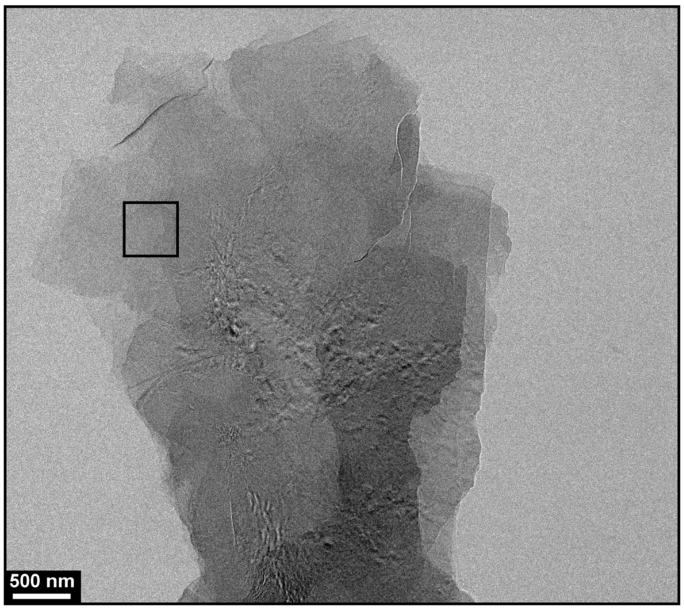

Extended Data Fig. 7 | Transmission electron microscopy image of graphullerene. The layered structure of graphullerene is apparent in this low-magnification image. Our best estimate for the number of layers within the selected area (black box) is 2–4 based on how the contrast increases stepwise from the edge of the flake towards the selected area.

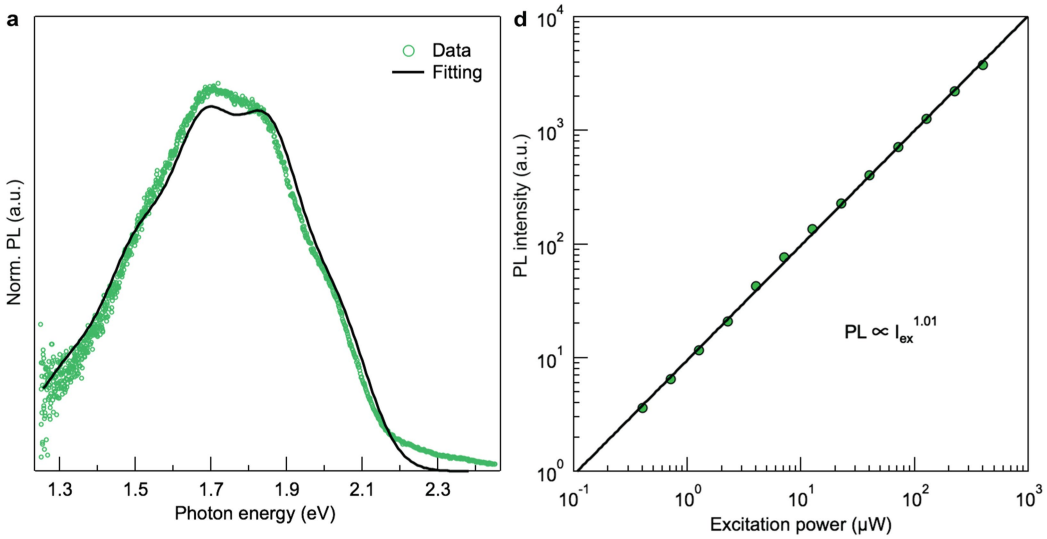

Extended Data Fig. 8 | Photoluminescence of $(Mg_4C_{60})_\infty$. a, The open circles represent the experimental data and the solid line is the fitting result based on the Franck–Condon model. **b**, PL intensity as a function of excitation laser power.

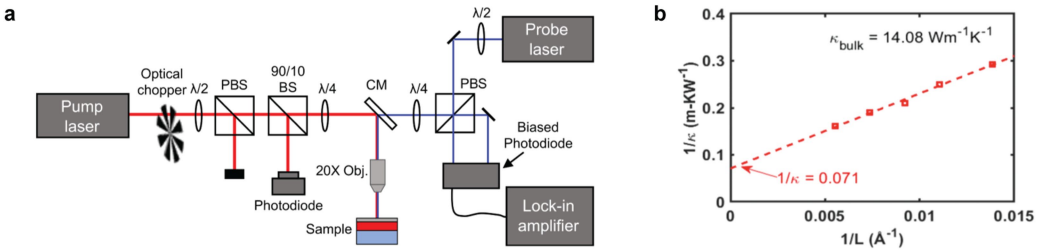

Extended Data Fig. 9 | Thermal property characterization. a, Thermal conductivity measurements on graphullerite were conducted using a fibre-based SSTR set-up similar to the schematic shown. **b**, The inverse of thermal conductivity versus the inverse of the simulation domain length.

Extended Data Table 1 | Crystallographic data for $(Mg_4C_{60})_\infty$

Chemical formula	Mg_4C_{60}
CCDC Deposition Number	2151576
Formula weight	817.88
Crystal system	Monoclinic
Space group	*C*2/*c*
R_{int} **(%)**	3.3
Z	4
Temperature (K)	100
a **(Å)**	17.522(1)
b **(Å)**	9.1603(5)
c **(Å)**	16.021(1)
α **(°)**	90
β **(°)**	105.145(7)
γ **(°)**	90
V **(Å^3)**	2482.2(3)
D_{cal} **(g/cm^3)**	2.189
Radiation (Å)	Cu Kα = 1.54184
μ (mm^{-1})	1.90
Crystal size (mm)	0.08 x 0.06 x 0.04
T_{max}/T_{min}	1.12
R_1/wR_2	7.64/20.62
Reflections	2374